remote sensing

MDPI

Article

Retrieval of Suspended Sediment Concentrations in the Pearl River Estuary Using Multi-Source Satellite Imagery

Bowen Cao [1], Junliang Qiu [2], Wenxin Zhang [1], Xuetong Xie [1], Xixi Lu [3], Xiankun Yang [1,4,*] and Haitao Li [1]

[1] School of Geography and Remote Sensing, Guangzhou University, Guangzhou 510006, China
[2] Department of Land, Environment, Agriculture and Forestry, University of Padova, Agripolis, Viale dell'Università 16, 35020 Legnaro, Italy
[3] Department of Geography, National University of Singapore, 10 Kent Ridge Crescent, Singapore 119260, Singapore
[4] Rural Non-Point Source Pollution Comprehensive Management Technology Center of Guangdong Province, Guangzhou 510006, China
* Correspondence: yangxk@gzhu.edu.cn

Abstract: Monitoring and quantifying suspended sediment concentrations (SSC) in estuaries such as the Pearl River Estuary (PRE) provide crucial information for environmental processes, hydrological infrastructure, and navigation. Traditional SSC mapping based on in situ investigations lacks the spatial coverage necessitated by detailed analysis. In this study, based on in situ spectral data and SSC measurements, we developed models to quantify SSC based on Landsat TM/OLI and Sentinel-2 imagery. The models were then used to map the SSC distribution in the PRE for the period 1986–2020. The results indicated that SSC in the entire PRE displayed an overall decreasing trend over the past 35 years, but an abnormal increase was also observed in shallow waters near Hengmen. Geographically, the concentration along the west coast is higher than on the east coast, and the central part of Lingding Bay underwent a slight increase. The decreased sediment output from the Pearl River Basin is the major cause of the decreasing changes in SSC. However, the natural factors and human activities such as channel dredging and the construction of artificial facilities can also disturb the spatial distribution of SSC. Regions with a significant decrease in SSC should have special concerns about retaining the PRE's health and sustainability.

Keywords: ASD spectrum; Landsat-8 OLI; Lingding Bay; suspended sediment concentrations; Mann–Kendall trend test; Pearl River estuary

Citation: Cao, B.; Qiu, J.; Zhang, W.; Xie, X.; Lu, X.; Yang, X.; Li, H. Retrieval of Suspended Sediment Concentrations in the Pearl River Estuary Using Multi-Source Satellite Imagery. *Remote Sens.* **2022**, *14*, 3896. https://doi.org/10.3390/rs14163896

Academic Editor: Assefa M. Melesse

Received: 13 June 2022
Accepted: 9 August 2022
Published: 11 August 2022

1. Introduction

Suspended sediments in the estuary are extremely important for the regulation of erosion-accretion and for constructing geomorphological patterns. Normally, the investigations of sediment concentrations (SSC) require various in situ observations at specific cross-sections; they, therefore, cannot provide an overall spatial view of the processes in positions excluding the monitoring stations, especially in estuary-like areas with high SSC fluctuation. That is extremely important because sediment transport in estuaries may severely affect estuary management and coastal protection regarding the economic and environmental significance of estuarine sediment transport.

Previous studies have reported the possibility of using satellite images as a complement to sediment observation networks [1,2] due to their wide geographical coverage, high time resolution, and potential employment as an SSC proxy [3]. Some researchers have displayed a positive mathematical correlation between SSC in waters and the corresponding spectral response [4]. Stumpf et al. proposed a general approach to determine SSC in the estuarine waters for use with satellite data [5]. The study proved the correlation of SSC with satellite reflectance based on Advanced Very High-Resolution Radiometer (AVHRR) sensors. Likewise, Zhang et al. [6]. Performed representative quantitative monitoring and

evaluation of suspended sediment in the Yellow River Estuary using Landsat TM and ETM+ images. Similar studies were also performed in the Yangtze River Estuary [7], the Pearl River Estuary [8], the Yellow River estuary [9], as well as the macro-tidal Yalu River estuary [10]. They demonstrated that SSC monitoring on the basis of satellite imagery is an effective way to investigate the patterns and changes of SSC across a large estuarine area at a suitable scale. However, as satellite images from individual sensors often cannot be guaranteed for large spatial scale or long-term studies, using multi-source satellite images for SSC retrieval is becoming increasingly popular among the academic community. For instance, Gholizadeh et al. [4] believed that multispectral satellite data are more suitable for monitoring water quality in large-scale waterbodies such as coastal waters and large lakes.

Regarding the retrieval approaches, nowadays, empirical analysis based on linear regression and multi-factor statistics are still widely used, while principal component analysis and artificial neural networks are also effective alternatives for prediction accuracy improvement. As an emblematic study, Peterson et al. [11] presented a predictive reflectance–SSC model using an extreme learning machine (ELM) method. This study demonstrated the benefit of ELM over traditional approaches for the retrieval of SSC based on satellite images and its potential to improve the ability to investigate water quality parameters along large fluvial systems. However, the prediction of low SSC in small waterbodies is still a challenging task for remote sensing [12].

The key application of mapping SSC is to provide the spatial and temporal variations and interpret possible causes of the changes. It is crucial for the areas with few in situ observations and the regions with sharp variations in land surface processes (i.e., Asia, Africa, and South America with fast and dense anthropogenic activities). For example, many researchers have studied the long-term fluctuations in SSC in the estuaries of large Asian rivers to manifest the anthropogenic and climate-driven modifications in their basins [8]. China's large river estuaries are pertinent representatives. In their related river basins, anthropogenic activities, such as deforestation, reforestation, land reclamation, irrigation, and construction of numerous large dams, have become increasingly common, dramatically affecting sediment transport to the estuaries in a direct and indirect way [13–17]. However, greater anthropogenic impacts, in fact, occurred in the delta regions. Rapid urbanization, the emergence of massive infrastructure, and land and water transportation development have dramatically modified the movement of suspended sediment in the estuaries.

These impacts have been reported by various studies. Based on Sentinel-2 and Landsat satellite imagery, Li et al. [18] measured the SSC distribution change over the past 20 years for the Yellow River Estuary and Bohai Bay. They illustrated the changes in human activities in the Yellow River basin and the corresponding impacts on estuarine SSC seasonal changes [18]. Similar trends were also observed by Gao et al. [19] in the Pearl River Estuary. Wu et al. [20] collected in situ data in the Yangtze River Estuary and simulated tidal-driven changes in SSC using the Geostationary Ocean Color Imager (GOCI) data. They pointed out that the tides in the estuary caused significant changes in the spatial distribution of high SSC. Wang et al. [8], based on the SSC distributions retrieved from 112 Landsat images obtained during 1987–2015, analyzed the spatial and temporal variations of SSC in the monsoon and dry seasons in six specific small regions of the Pearl River Estuary (PRE). However, for estuaries in tropical and subtropical regions, SSC mapping is somewhat complicated, as satellite imagery is often unavailable because of the year-round high cloud coverage. The long-term change patterns of SSC movement and migration remain unclear.

The Pearl River Estuary is surrounded by a metropolitan area of the Guangdong–Hong Kong–Macao Greater Bay Area. It nourishes 11 cities, including Hong Kong and Macau, with a total population of about 63.7 million. Suspended sediment balance is extremely important for maintaining coastal stability, infrastructure security, and navigation safety. The Guangzhou Port, Shenzhen Port, and Hong Kong Port, located in the estuary, rank fourth, fifth, and ninth among the top ten busiest ports in the world. This study, taking the PRE as the study area, aimed to: (1) investigate the spatial patterns of SSC distribution across the PRE; (2) explore the spatio-temporal variation in SSC over the past 25 years;

(3) analyze the influencing factors of these changes in SSC and their relationship with human activities. The PRE is a key natural resource provider for the Guangdong–Hong Kong–Macau Greater Bay Area, which is also referred to as the Greater Bay Area (GBA). It nourishes approximately 71.2 million people located in the GBA. Further, the PRE is the major shipping lane from and to the GBA for the international maritime trade via the South China Sea. A large part of the PRE has been designated as a national nature reserve as an important habitat for the Chinese white dolphins (the Indo-Pacific humpback dolphin). Therefore, this study is valuable for accurately understanding the environmental changes and promoting the sustainable development of the PRE.

2. Materials and Methods

2.1. Study Area

The Pearl River, China's second largest river, consists of the West River, North River, and East River. The outlets of the West River, North River, and East River are Gaoyao station, Shijiao station, and Boluo station, respectively (Figure 1). Located in southern China, the river nourishes the Pearl River Delta with a dense river network. In the Pearl River Basin (PRB), the average annual runoff in the past ten years is 285 billion m^3 yr^{-1}, and the average annual sediment transport in the past ten years is 23.13 million tons yr^{-1} (Table 1). According to the latest official report from the Pearl River Commission, the hydraulic erosion area reached 80,800 km^2, which is approximately 18.31% of the total area of the Pearl River Basin (441,400 km^2).

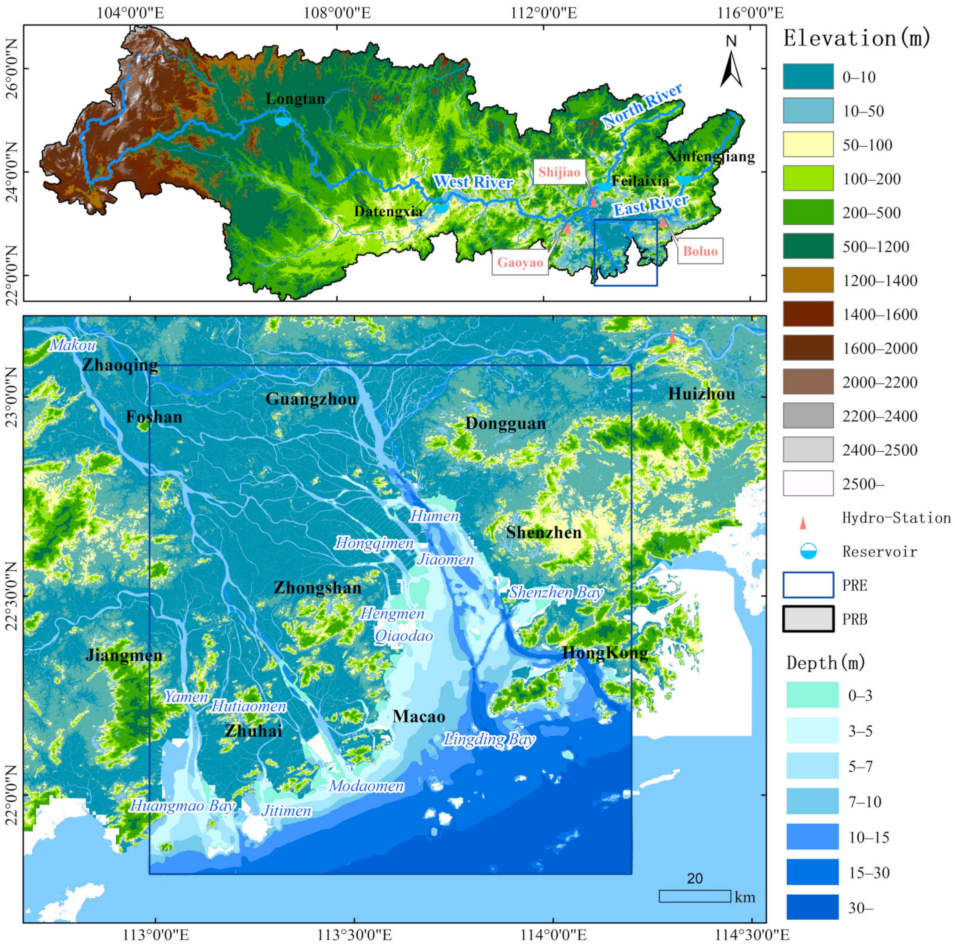

Figure 1. Geographical map of main streams of the Pearl River and spatial configuration of PRD.

Table 1. Basic information on runoff (10^8 m^3) and sediment load (10^4 t) of the Pearl River.

Year	Type	Gaoyao	Shijiao	Boluo	Total of PR
Average from 1954 to 2020	Runoff	2186	417.8	232	3419
	Sediment load	5650	525	217	7400
Average in the past 10 years	runoff	2212	421	223.7	-
	Sediment load	1740	464	91.4	-
2019	runoff	2397	537.1	270.6	3972
	Sediment load	2460	488	160	3320
2020	runoff	2173	364	157.1	3085
	Sediment load	1830	404	44.3	2770

The West River is the longest tributary, with a length of 2075 km and an altitude difference of more than 2100 m. According to the observations at Gaoyao station in 2019, sediment transport from the West River is more than 17.2 million tons yr^{-1} or 74.36% of the total sediment from PRB. However, considering the soil erosion intensity of 127 tons km^{-2} in 2019, soil loss in the North River could be more severe than in the West River and East River. For this cause, the local government has enhanced soil and water conservation.

Unlike other temperate Chinese estuaries (e.g., the Yellow River Estuary), the average tidal range in the PRE is relatively small in the offshore waters and increases gradually towards the estuary, reaching the peak in the upstream part of the estuary. The distribution of the mean current is also manifest in unique characteristics: freshwater was dominant on the western side, while saltwater was dominant on the opposite side. The main components of the current in the estuary were the river flow, saltwater intrusion, and tidal currents [21]. In the northern part of the estuary, the tidal currents are rectilinear, and the river discharge dominates the non-tidal currents. However, in the west part of the estuary, the outflow from the three river outlets is much stronger than in the northeast. In the Southeast of Lingding Bay (Figure 1), the tidal currents are rotary, and the river outflow dominates the non-tidal currents in the top layer, while the saltwater intrusion dominates the lower layer.

The suspended sediments in the Pearl River Estuary mainly come from the Pearl River Basin, outputting sediments via eight outlets (Figure 1), the coastal area via wind-driven sediment resuspension, and a few from marine sediment input. There are several crucial outlets for the output of upstream runoff and sediments to the estuary. The Modaomen (Figure 1) is the major outlet for 25.0% of water discharge and 36% of the sediment output. Approximately 40.0% of the total water discharge and sediment load are released via the outlets of the Hengmen, Hongqimen, and Jiaomen into the west part of the PRE. In the past decades, the output sediments from the Pearl River Basin have experienced a dramatic decrease from nearly 90 million tons in the 1990s to the present 25 million tons only [22]. In the monsoon season, due to the large runoff and high SSC from the Pearl River, the SSC near the west coast is relatively high, with an SSC of 0.2–0.4 kg/m^3. In the east part, however, as the Humen outlet receives runoff from the East River with quite low SSC and the tidal flow is large, the SSC is often as low as 0.1–0.2 kg/m^3. At the end of the east Lingding Bay, due to the intrusion of saltwater, the SSC decreases to below 0.1–0.05 kg/m^3. In the dry season, the SSC on the west coast is approximately 0.2–0.3 kg/m^3; in the east part, the SSC is even less than 0.05 kg/m^3 due to the sharp decrease in sediment intake. However, during high tides, due to marine sediment input, the SSC in some areas can slightly increase to 0.05–0.15 kg/m^3, but the SSC in the east waters is still much lower than in the west.

In the PRE, the spatial distribution of SSC is also affected by seasonal winds. In winter, the estuary is dominated by strong northeast winds. Due to the interplay of strong northeast winds and south tides, the suspended sediment along the north coast can be fully mixed; the suspended sediment is thus distributed in a more even way. In summer, the estuary is controlled by southwest winds, which will cause seasonal upwelling on the southwest side of the estuary, leading to the resuspension of sediments [23]. This is also an important effect on the high SSC in summer.

2.2. In Situ Data Collection

This study conducted four field investigations in the PRE to collect in situ spectral data and corresponding water samples for later SSC measurements in the laboratory. Considering high cloud coverage over the PRE, we executed field surveys in cloud-free conditions one day before or after the visiting date of the Landsat 8 satellite over the study area. The fieldwork was performed in July 2020, December 2020, April 2021, and July 2021. The spectral data were measured using the Analytical Spectral Devices (ASD) FieldSpec 4, provided by the ASD Company, based on the above-water hyperspectral remote sensing reflectance (R_{rs}) from NASA-recommended protocols [24]. The sampling routes and locations were selected in a random way. Finally, 115 samples were collected, but only 108 of which are valid. Other samples were considered as invalid as spectral data were incorrectly collected in an overexposed condition. Meanwhile, two bottles of 500 mL water were collected at each sampling site for later laboratory analysis for suspended sediment concentration and other physicochemical factors (not considered in this study). The water samples were immediately stored in a mobile fridge to avoid physicochemical changes in samples. Auxiliary environmental information, such as longitude, latitude, wind speed, and other ambient environmental factors, were also documented for later data processing (i.e., matching the Fresnel reflectance of the water surface for the R_{rs} calculation).

Water sample collection and processing are vital for the estimation of SSC. The special data were analyzed according to FieldSpec 4 instrument operating instructions and study by Tang et al. [25]. To guarantee the water sample data quality, the water sample collection and processing were performed on the basis of these rules: First, the sampled SSC values should have a statistically normal distribution. Second, the difference for the double measurements of the weight of a filter paper should be within 0.5 mg, and the filter paper needs to be weighed at least twice before and after filtration. Lastly, the sediment retained by each filter paper should exceed 10 mg but not exceed 100 mg.

The above-water measurement method was used to collect spectral data. Figure 2 shows that to avoid perpendicular sunlight input, the hand-held ASD Spectroradiometer should be positioned over the water surface at an angle of 45° or 135°. Because the incident light received by the fiber optic probe includes scattered light from the sky and reflected light from the ambient environment, it needs to be calibrated with a reference panel. The ASD spectral data were then processed to obtain accurate reflectance.

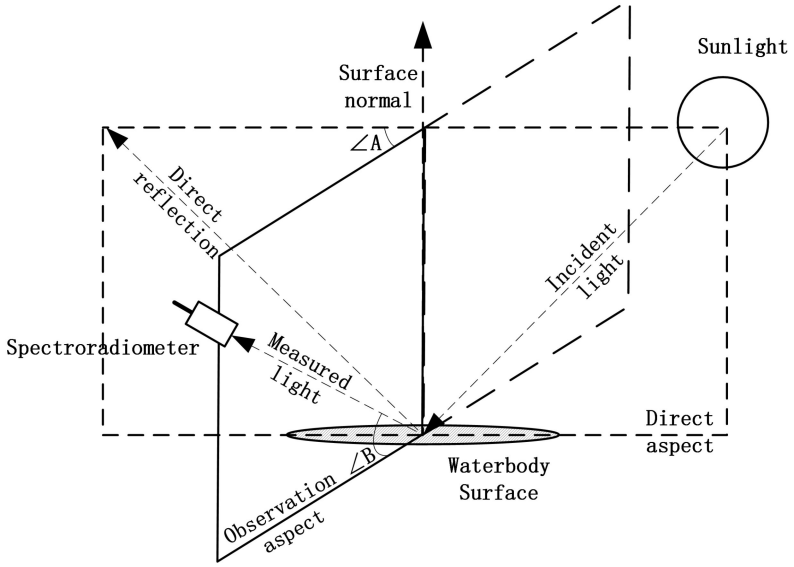

Figure 2. Reflectance data collection using the above-water measurement method. The water samples and the spectral data collected by the ASD FieldSpec 4 were obtained at the same location.

2.2.1. Normalized Water Surface Reflectance

The White Reference (WR) or Reference Panel called Spectralon is an important part of calibrating incident light intensity. Because the spectroradiometer only measures the instantaneous intensity of a specified light field. However, the reflectance is an apparent optical property of the waterbody, dependent on the light source. To measure solar radiation at different times, places, and incident angles, taking a WR measurement is required. The reflectance of the WR is used as a known condition for the calibration. According to Equation (1), the water surface reflectance can be calculated [24]. The R_{rs} is generally considered to be the real reflectance with environmental influences removed, which is also called the normalized water surface reflectance.

$$R_{rs}(\lambda) = \frac{L_u(\lambda) - L_{sky}(\lambda) * r_{sky}}{L_p(\lambda) * \frac{\pi}{\rho_p(\lambda)}} \quad (1)$$

where λ is the wavelength with a range of 350–2500 nm, its width is resampled as 1 nm. $L_u(\lambda)$ is the upward radiance from the water surface, $L_{sky}(\lambda)$ is the downward radiance of the skylight, $L_p(\lambda)$ is the radiance of the WR, and $\rho_p(\lambda)$ is the reflectance of the WR. Based on the wind speed and the zenith angle, the azimuth angle (calculated from latitude, longitude, and time) of the observation point and r_{sky} the sky light reflectance is determined in the lookup table.

2.2.2. Spectral Characteristics of Turbid Waters

In the spectrum curve of turbid waters (Figure 3), the reflectance displays an increasing trend with the increase in SSC. Its typical range indicating significant changes is 550–800 nm. Normally, the first reflection peak happens at approximately 580 nm. The reflectance decreases abruptly after 700 nm, showing absorption characteristics. In more turbid water bodies, the sensitive band range is broadened, resulting in spectral differences in the range of 650–700 nm. This difference can be amplified by band operation, highlighting the sensitivity to changes in SSC, which is the theoretical basis for SSC retrieval-based multi-band sensors.

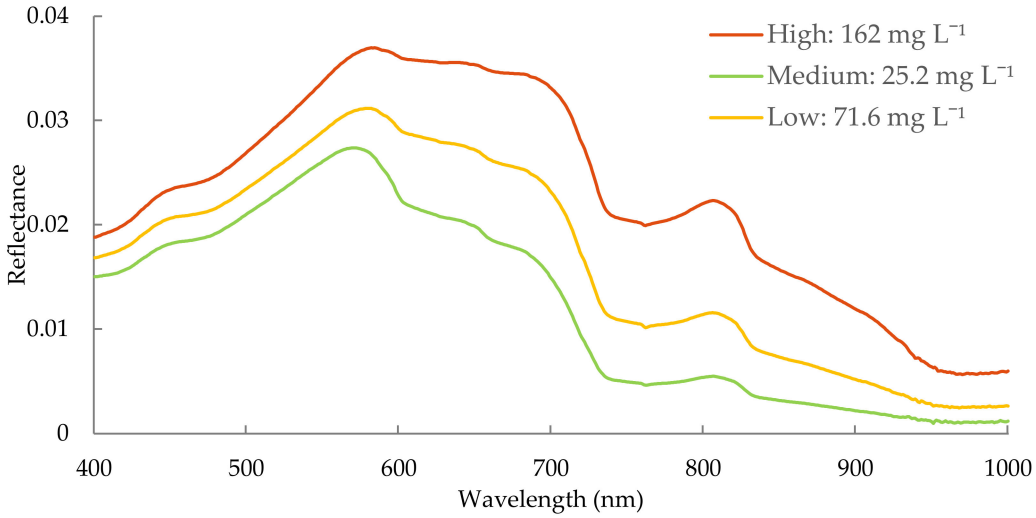

Figure 3. Spectral reflectance curve of turbid waters, reflectance changes with SSC fluctuation.

If the SSC is low, the change in chlorophyll concentration will play a greater role in the regulation of water reflectance. In the range of 690–710 nm, there is a fluorescence peak that changes with the chlorophyll concentration [26]. The bands are not recommended for SSC retrieval using satellite imagery. Generally, the red band with the range of 650–670 nm is the first option, and the combination of the blue band of 450–500 nm can further reduce

the influence of chlorophyll. Some studies have shown that the combination of the red and green bands is also effective [27–29].

In previous studies [30,31], the red band of multispectral images is generally considered the major band for SSC estimation. Similar conclusions can be drawn from the sensitive band analysis based on the in situ measured spectrum. In addition, different band combinations were often used with the advantage of reducing atmospheric effects. For example, differences in sensors, weather conditions, or preprocessing methods could result in uncertainty in reflectance. According to the results of band correlation analysis, the correlation coefficient of *B*4 is 0.73. The combination of *B*3 and *B*4 was used as the independent variable: $(B3 + B4)/(B3/B4)$, and its correlation coefficient is 0.8.

2.3. Satellite Data and Image Pre-Processing

2.3.1. Satellite Data Availability

The Landsat satellite series is an important free satellite image provider. They have been used by many studies for SSC retrieval. Here, the long-term Landsat images were used for mapping SSC spatial distribution across the PRE. Landsat-5 TM (1985–2011) and Landsat-8 OLI (2013–2020) images series are from USGS (https://www.usgs.gov/, accessed on 1 July 2021). The images are all visually screened to ensure less cloud cover in PRE. However, regarding the subtropical climate characteristics (Figure 1) and resultant high cloud coverage in the PRE, Sentinel-2 images (2015–now) were also used to complement the missing Landsat images. The Sentinel-2 satellite images, coming with a higher spatial and temporal resolution, are a desirable alternative for Landsat images. The visible light band (10 m resolution) was selected based on the wavelength response characteristics. The optional bulk data download service (BDA 2.0), available after recent updates of the USGS website, was used for image acquisition. Using the tool, researchers can also download the desired bands only. The total number of Landsat images in the past 35 years (1986–2020, except 2012) is 225 scenes, including 170 scenes from Landsat-5 TM and 55 scenes from Landsat-8 OLI. The remaining are alternative Sentinel-2 images. For Landsat images, all were obtained with Path/Row coordinates of (122,044) and (122,045).

As can be seen from Figure 4, there are few satellite images available during the monsoon season from March to June. During the dry season, especially in October, November, December, and January, more satellite images are available and of good quality for SSC retrieval. Therefore, in the latter image analysis, the results for the monsoon season could be affected due to insufficient images obtained from March to June. It can also be seen that in 2012, no satellite imagery was available for the whole year.

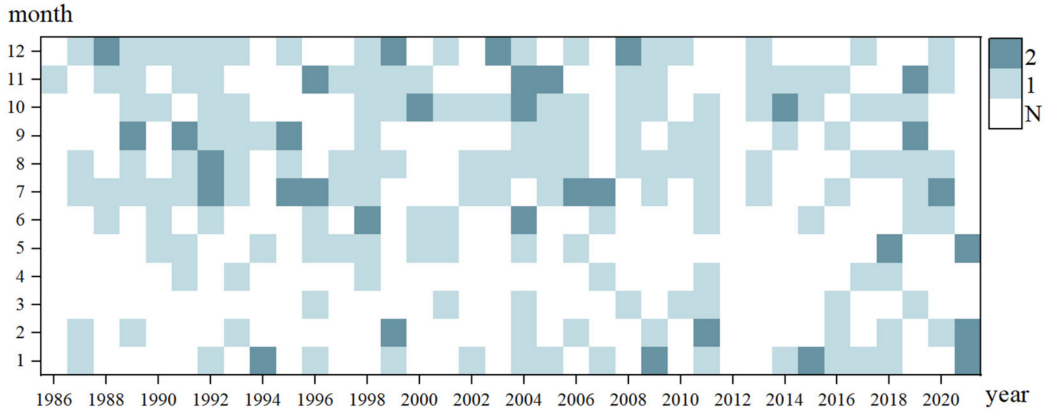

Figure 4. Monthly availability of Landsat and Sentinel-2 images for SSC mapping. (N refers to the unavailability of images in the specific month, the color depth represents the number of images in the corresponding month, and the dark color represents two scene images available).

2.3.2. Satellite Image Correction

The preprocessing procedure includes atmospheric correction and cloud removal. Figure 5 is the image processing workflow. There are three major radiative transfer models for widely used correction algorithms, namely, the MODTRAN4+ model in FLAASH, the 6S model in LEDAPS, and the internal model in LaSRC. LaSRC and LEDAPS are officially provided by the USGS and integrated into Landsat Collection 2 Surface Reflectance (SR) products. Before the image processing procedure, the most appropriate algorithm was used based on model performance assessment. For the Landsat-5 TM series, the opensource 6S model was used to obtain the SR. The corrected results were compared with the LEDAPS algorithm from USGS. Then, the images with high cloud coverage were removed. The LaSRC model was verified with the most accurate correction results for OLI images. After comparative testing, using FLAASH and LEDAPS correction methods, the reflectivity error is less than 0.005. Sentinel-2 MSI series were corrected using the model integrated into the batch processing tool, named the Sen2Cor provided by ESA.

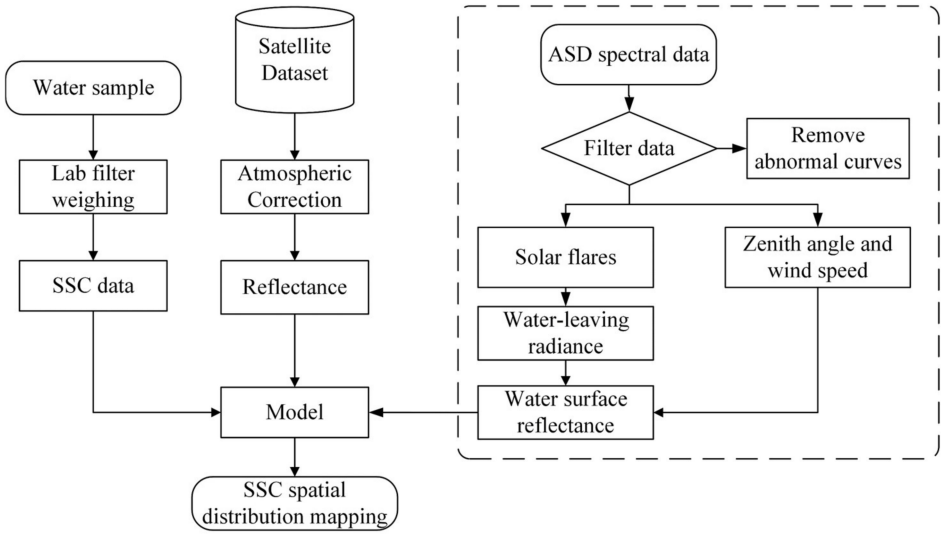

Figure 5. Image retrieval workflow with integrated satellite images and field data.

In previous studies, the ASD in situ spectrum is the reflectance at all wavelengths of 350 to 2500 nm. The satellite data and the ASD data are matched via a convolution operation [12]. For example, for band4 (Wavelength: 636–673 nm) of Landsat-8, the convolution equation is as follows:

$$R_{rs}(\lambda) = \frac{\sum_{i=1}^{n} R_{rs}(\lambda_i) \times RSR(\lambda_i)}{\sum_{i=1}^{n} R_{rs}(\lambda_i)} \quad (2)$$

where $R_{rs}(\lambda)$ is the reflectance at images wavelength λ. λ_i is the upper and lower limits of the bandwidth, n is the number of bands within the band range, and $RSR(\lambda_i)$ is the spectral response function of the satellite sensor.

The reflectance values for waters are often distributed between 0.05 and 0.12, which is slightly different from the in situ measured spectrum. The slight discrepancy can be corrected using the model proposed by Chelotti et al. [12] based on the SWIR band. The proposed model can be expressed as follows:

$$R_{rs}(\lambda) = \frac{R(\lambda) - min(R_{NIR} : R_{SWIR})}{\pi} \quad (3)$$

In the formula, the reflectance $R(\lambda)$ is subtracted by the smallest value between the near-infrared (*NIR*) and short-wave infrared (*SWIR*) bands. The pixel-based correction process is for normal pixel values of the two bands. Negative or abnormal values for both

bands were considered invalid pixels. The subtraction result was divided by the coefficient π to obtain the corrected reflectance $R_{rs}(\lambda)$. The SWIR-based correction method is on the basis of two assumptions [32]: (1) The lowest reflectance between the NIR band and the SWIR is the residual reflectance or noise caused by atmospheric aerosol scattering, skylight reflection, etc. (2) The noise does not change with wavelength.

Figure 6 shows an example of using the Landsat-8 mid-infrared band to correct visible light bands (*B*2, *B*3) and near-infrared bands (*B*4, *B*5, *B*6). The calibration results preserved the main relationship between these bands, and the reflectance distribution interval is consistent with the ASD in situ spectrum.

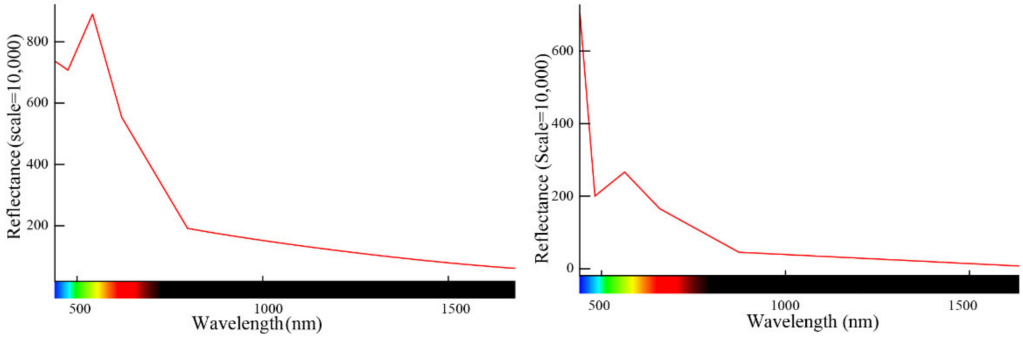

Figure 6. Corrected results of water surface reflectance for Landsat-8 imagery.

2.3.3. Mann–Kendall Trend Test

The Mann–Kendall Trend Test (also called the M-K test) is often employed to measure a dataset collected over time for consistently increasing or decreasing changes. The test is a non-parametric test, which means it can perform for all distributions (i.e., the data does not have to meet the assumption of normality). Here we used the M-K test to examine the temporal variation of the SSC at each pixel. The M-K test can be expressed as follows:

$$S_k = \sum_{k=1}^{n-1} \sum_{j=k+1}^{n} \mathrm{Sgn}(\mathrm{X}_j - \mathrm{X}_k) \tag{4}$$

$$UF_k = \frac{S_k - E(S_k)}{\sqrt{Var(S_k)}} \tag{5}$$

where $\mathrm{Sgn}(\mathrm{X}_j - \mathrm{X}_k)$ is an assignment function that sets the positive or negative values to 1 or -1. $UF_k (k = 0, 1, 2, 3, \ldots, n)$, $E(S_k)$ is the mean, $Var(S_k)$ is the variance; when UF_k is greater than 0, the performance increases; otherwise, it indicates a decreasing trend. UB_k represents the reverse time order ($k = n$, $(n-1)$), $\ldots$, 1).

The $RMSE$ root mean square error was used to test the model performance, and the relative error (RE) test was computed too.

$$RMSE = \sqrt{\frac{\sum_{i=1}^{n} (y_i - y_i')^2}{N}} \tag{6}$$

$$RE = 100 \times \frac{1}{n} \sum_{i=1}^{n} \frac{|y_i - y_i'|}{y_i} \tag{7}$$

where y_i' is the real measured value, y_i is the predicted value, and n is the number of samples. Smaller $RMSE$ and RE means smaller error and better fitting performance.

2.4. Hydrological Observations and Meteorological Data

Sediment load data at the hydrological stations of Gaoyao, Shijiao, and Boluo were also collected to verify the predicted SSC at these stations [33]. The spatial distribution of

the four stations is shown in Figure 1. The data were officially provided by the Pearl River Commission, including continuous daily sediment records from 2012 to 2018. The monthly sediment discharge and runoff from 2002 to 2020 were released by the Ministry of Water Resources, which were used to observe the periodic changes in sediment load and runoff.

3. Results

3.1. Spectral Characteristics of Turbid Water

The water surface reflectance was obtained after the spectral curve in Figure 7 was corrected. Before fitting the in situ SSC data to the satellite reflectance, the model of Formula (2) was used for preprocessing. The spectral value was calculated according to the sensor's spectral response function. The model used for fitting the in situ SSC data to the satellite reflectance is the natural logarithmic model. As the difference between the values of the independent variable and the dependent variable could be as high as several orders of magnitude, to avoid deriving extremes from the model, we first proceed with the satellite reflectance and the measured reflectance using min-max normalization. Then, the two series were input to establish a fitting formula. When the reflectance of a pixel is known, the corresponding SSC can be mapped using the model.

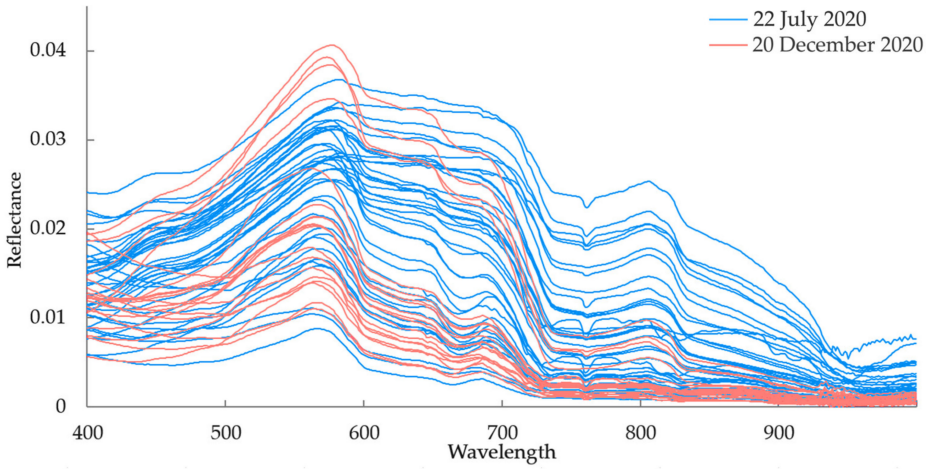

Figure 7. Field-measured spectral series of R_{rs} collected on 22 July and 20 December 2020.

Table 2 shows the partial ASD in situ SSC data collected in the summer (July) and winter (December) of 2020 (all data are shown in Appendix A). Spectral data collection and water sampling collection were performed at the same time and the same location to guarantee data consistency.

Table 2. SSC data analyzed in the laboratory.

ID	Sediment (mg)	Filter Paper (mg)	Sample Weight (mL)	SSC (mg L^{-1})
1	85.1	131.7	300	278.0
2	70.7	131.3	300	232.3
3	87.1	132.5	300	288.0
4	65.4	132.7	500	129.8
5	50.8	132.1	300	167.7
6	66.4	131.2	350	189.7
7	54.1	131.4	300	179.0
8	30.9	133.5	300	103.0
9	48.6	131.6	300	162.0
10	42.3	132.9	500	84.6
11	24.1	131.4	300	80.3
12	16.4	133.4	300	54.7
13	16.0	131.1	300	53.3

The natural logarithmic model based on in situ spectral reflectances (matched to OLI band4) and measured suspended sediment data is shown in Figure 8.

$$SSC = 3.501 * e^{4.317 * R_{rs}} \quad (8)$$

where R_{rs} is the water reflectance and SSC is the total suspended sediment concentration. When the SSC is not too high (<200 mg/L), the model worked well. In addition, the model is simple, and its parameters are easy to obtain. Only when the SSC exceeds 200 mg L^{-1} does the fitting accuracy will decrease slightly. After removing invalid data, we randomly selected 39 samples for modeling, and the remaining were used for error testing.

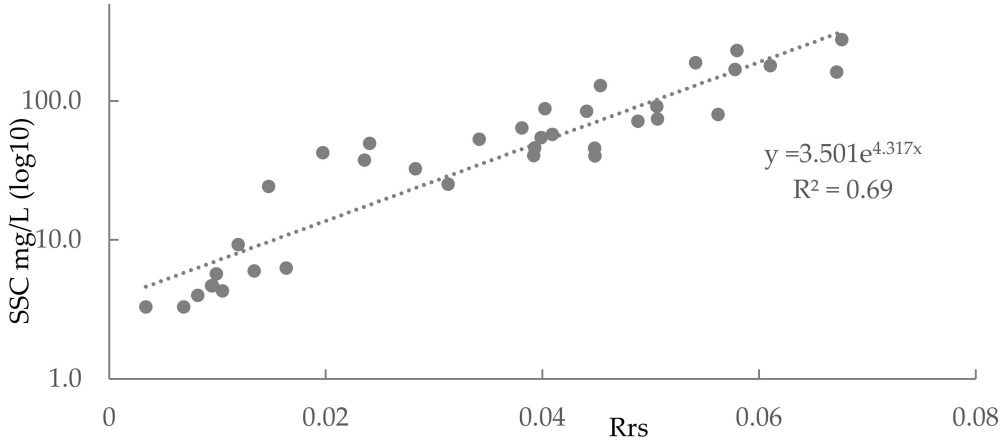

Figure 8. Simulated natural logarithmic model between in situ spectral data and measured SSC, and the main reflectance is between 0.02 and 0.06, matched to the OLI's Band 4, and the corresponding sediment data is 4–189 mg L^{-1}.

In Table 3, the band is the observed reflectance corresponding to wavelengths of the OLI sensor to compare the response of different models to wavelengths. The TM sensor and the MSI sensor were also compared, with minor differences between the models. Thus, the same model was used in the retrieval.

Table 3. The test results for the model accuracy evaluation.

Band	Models	R^2	RMSE	RE
Landsat OLI *B*4	y = 189.87x − 40.873	R^2 = 0.55	21.29	95.07%
	$Y = 3.501e^{4.317x}$	R^2 = 0.69	8.28	18.98%
Landsat OLI (*B*3 + *B*4)/(*B*3/*B*4)	y = 195.67x − 26.19	R^2 = 0.70	26.63	84.90%
	$y = 4.6e^{4.227x}$	R^2 = 0.79	7.17	17.62%

3.2. Spatial Patterns of SSC in PRE

Overall, the multi-year average SSC presents a significant spatial pattern of being high on the west coast and low on the east coast across the PRE (Figure 9), with the highest concentration from the northeast to the southwest coast and gradually decreasing from the southwest to east. On the west coast, at the junction of Guangzhou and Zhongshan cities, the high SSC values occurred at the outlets of Hongqimen and Hengmen due to high sediment out at these outlets, as approximately 40.0% of the total water discharge and sediment load is released via the outlets of the Hongqimen, Hengmen, and Jiaomen into the west part of Lingding Bay.

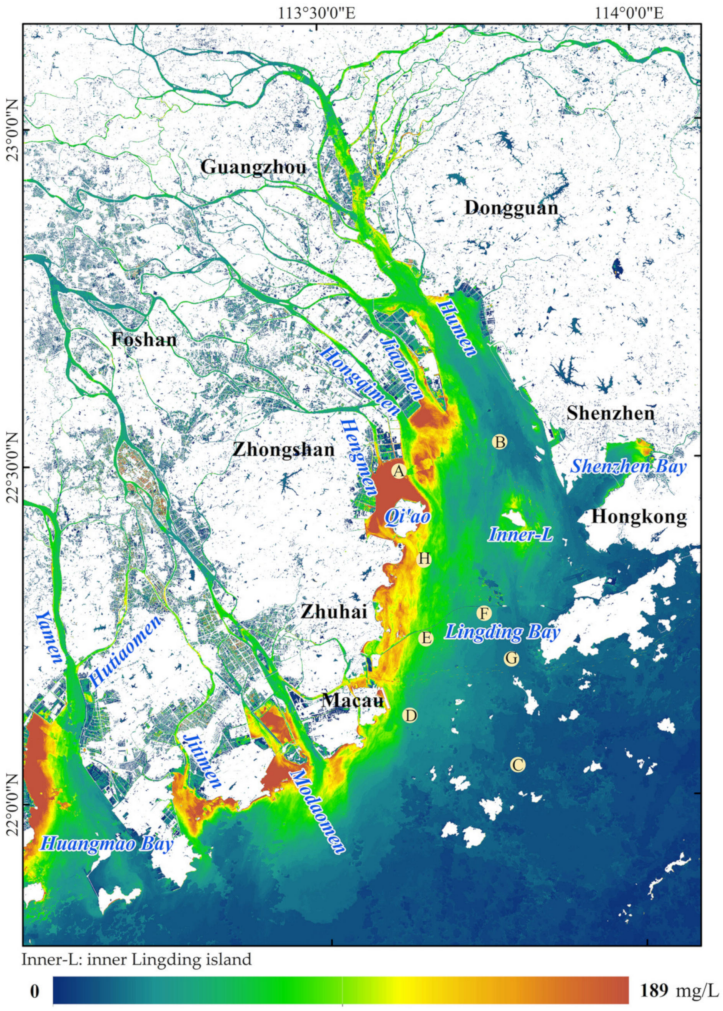

Figure 9. Spatial distribution of the multi-year average of SSC retrieved from Landsat-8 OLI. (A–H) are eight major monitoring locations selected according to SSC distribution.

The suspended sediment turbidity zone is formed in Humen and Jiaomen along the coast from Hongqili, Hengmen, to Maodaomen. At other outlets of the West River, such as the area from the outlets of Maodaomen to the Huangmao Bay, a high SSC region was also observed due to the large sediment output from the West River. Along the east coast, due to the relatively lower SSC from the East River and the confluence of many small streams into the main estuary, clearer water is formed near the city of Shenzhen. However, a relatively high SSC was also observed in Shenzhen Bay due to the high anthropogenic impacts. Downstream of Qi'ao Island, the suspended sediment washed into Inner Lingding Bay with the fresh water to form an area with high SSC concentration but decreased rapidly in the direction toward the end of Lingding Bay. The low-SSC area on both sides of Inner Lingding Island is actually the major waterways, where the SSC is influenced by the combined impact of water flow from the Pearl River and the dredging operation along the waterways.

3.3. The Long-Term Changes of SSC in PRE

Based on Landsat OLI image data for the last 8 years, the SSC distribution was retrieved (Figure 10), and the average value for each year was extracted to analyze the overall interannual variations in SSC. Sentinel-2 images were resampled to 30 m to supplement the missing data for the last five years. The results of four seasons in 2020 were taken to analyze the seasonal variations. Subsequently, the long-term variations over 35 years were analyzed by combining the long-term results obtained from Landsat and Sentinel images.

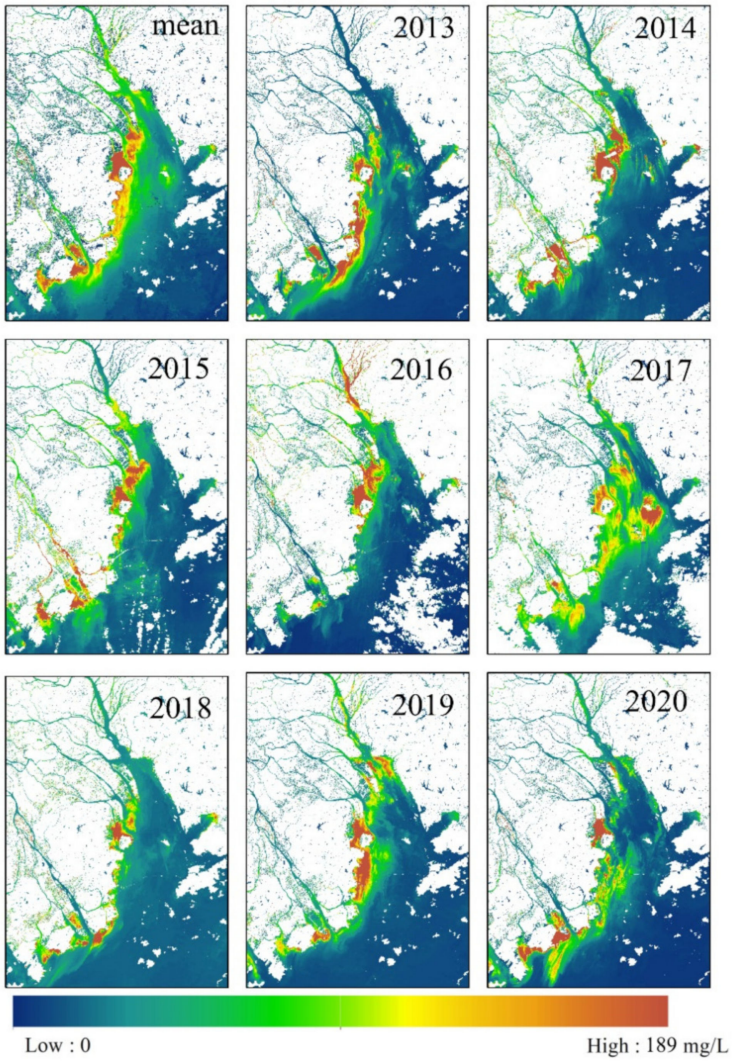

Figure 10. Annual SSC distribution for the years 2013–2020 based on Landsat-8 images. The mean map is the average of the 8-year SSC distribution.

3.3.1. The Distribution of Multi-Year Average SSC

The SSC distribution for 8 years since 2013 is shown in Figure 10. The annual average distribution reflects that the overall pattern of SSC distribution in the PRE remains consistently high on the northwest coast and low on the southeast coast. The large amount of sediment carried by the West River is the main contributor to the high concentrations outside the outlets along the west coast. It can be seen that the area with high SSC values in Inner Lingding Bay was much larger in 2017 (Figure 11).

Combined with runoff data, we can identify the flood that occurred in the summer of 2017; the runoff in June is 127% of the runoff in the same month of 2016. The runoff increased by 24.98 billion m^3 during the same period of March–September, carrying 14.981 million tons of sediment, a large amount of which was bought to the estuary, directly causing the high SSC distribution in the PRE in 2017. It can also be seen that, in 2016, the floods in the East River Basin directly caused a significant increase in the SSC at the outlet of the East River and in the mainstream just upstream of Lingding Bay. Overall, the three major tributaries of the Pearl River remain the major sources of sediment for the PRE. The fluctuation of SSC is largely controlled by upstream sediment output.

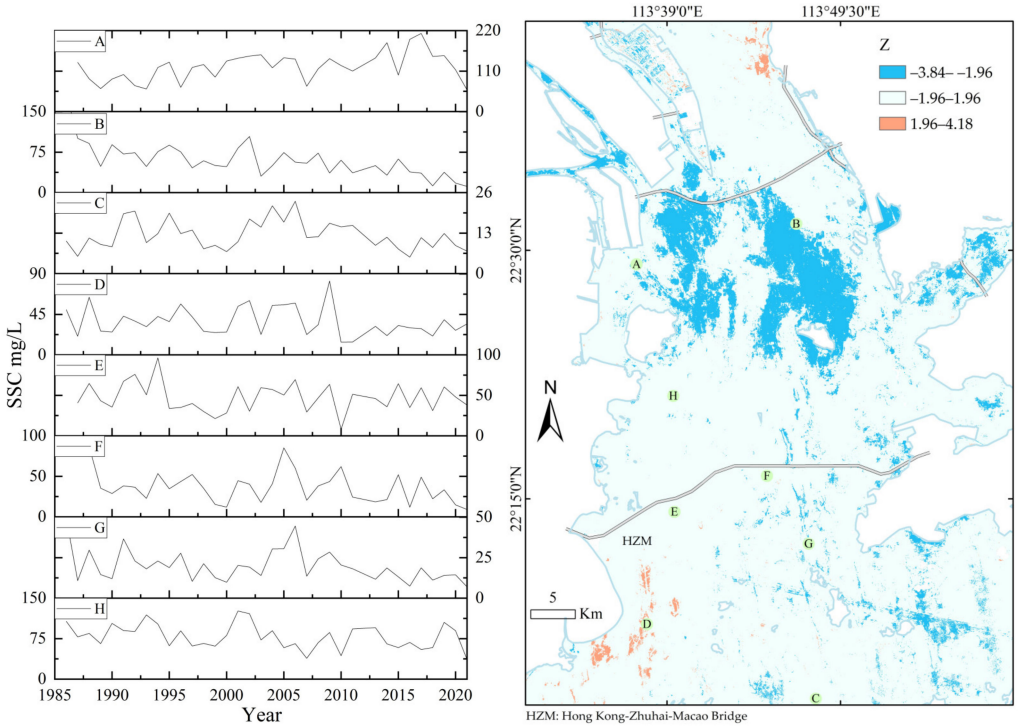

Figure 11. Long-term changes in SSC for the period 1986 to 2020 based on Landsat TM/OLI and Sentinel images (**left**); Z-statistic distribution of the long-term SSC change based on the M-K test (**right**).

3.3.2. Mann–Kendall Test Results

The SSC was mapped based on Landsat TM and OLI with a total of 300 images. Eight major monitoring locations were selected (see Figure 11) to make deep investigations into SSC variations according to the spatial characteristics of SSC. Figure 11 left shows the temporal change of the SSC distribution for the eight monitoring locations. Over a period of 35 years, the trends in different regions of the PRE were somewhat similar, with most regions showing an overall decreasing trend. Monitoring at locations B, D, F, G, and H showed a significant downward trend from the 1980s to the end of the 20th century, with locations B and G showing the most pronounced downward trend. These sites are all located along the west coast of the PRE, as the sediment from the Pearl River Basin into the sea is the major sediment source of SSC at the sites.

Moreover, there were also high fluctuations in SSC at almost all monitored locations between 2001 and 2006, as there were floods in both 2004 and 2005, resulting in higher SSCs in these two years. It can be seen that the decreasing trend became more significant after 2006. Considering the closure of the Longtan Reservoir on the main stem of the West River, with a storage capacity of 27.3 billion m^3, most of the sediment from the middle and upper reaches is trapped in the reservoir, and the lower sediment transport from the West River was obtained, leading to lower SSC in the PRE. It should be noted that site A displayed an overall opposite trend with a significant increasing trend in SSC. The possible cause is that this side, behind Qi'ao island, received the slower flow and resultant frequent siltation. The long-term siltation has created a large shallow water region near site A, with a water level of less than 3 m; hence this region is also known as the "Hengmen beach". Further, downstream of Hongqimen channel, which is the main reclaimed land area in Guangzhou's Nansha District, the rapid expansion of land has caused a decrease in average water level to around 3 m, while the underwater reflection causes water color changes, which may impact the final SSC retrieval.

Based on the M-K test results, Figure 11 (right figure) shows the total change trend in the estuary. The Z-value is an evaluation index for change of the time series data, which uses an annual average SSC distribution map. Site A showed a significant increasing trend

with a confidence level of 99%, while site B showed a decreasing trend at a confidence level of 99% too. Site H showed a decreasing trend at a confidence level of 90%. Sites B, C, D, and E showed a decreasing trend, but none of them reached a 90% confidence level (Table 4).

Table 4. M-K test for the SSC change at eight specific sites.

Point Name	Trend	P	Z
A	increasing	0.01	2.57
B	decreasing	0.001	−4.18
C	no trend	0.42	−0.80
D	no trend	0.37	−0.88
E	no trend	0.57	−0.56
G	no trend	0.14	−1.48
H	decreasing	0.09	−1.71

We used the M-K test to analyze the results of SSC mapping in the entire PRE to evaluate its spatiotemporal trend across the PRE. Considering the high cloud coverage in the monsoon season, the cloudy and cloud shadow pixels will change the final test results, so the images for the dry season during November and February were selected to analyze the long-time variation trend. Compared with the one-dimensional data series in Figure 11, this test can determine the spatial patterns. The spatial distribution of Z-statistics indicated some significant decreasing regions in the middle region between Qi'ao Island to Inner Lingding Island and the increasing region along the Hong Kong–Zhuhai–Macao Bridge in the middle region of downstream Inner Lingding Bay. The most significant change is the area along the coasts of the outlet near Jiaomen, with confidence levels ranging from 85% to 99% in the red areas.

Based on the four monitoring sites with a high confidence level, the SSC characteristics of different areas of the PRE were analyzed. Generally, the SSC at site A was the highest, with a multi-year average value of 121.84 mg L^{-1}; the corresponding SSC at sites B and H were 60.2 and 78.68 mg L^{-1}, respectively. Moreover, because site G is the farthest from the shoreline, the SSC value at site G is also the lowest (19.93 mg L^{-1}). Only site A showed an increasing trend in SSC changes. The distribution of the UF and UB values for the trend analysis are as follows.

In the trend analysis for sites A, B, G, and H (Figure 12), both A and B have significant turning points. The turning point for site A occurred in 1998. The turning point B occurred after 2007. The trend for site B showed an insignificant decreasing trend at the beginning, followed by a significant decreasing trend after 2007. Site G showed a significant increasing trend and a quick decrease after 2007. The decrease for site G happened after 2013, and the turning point appeared around 2017. Location H showed an increasing trend at the beginning, fluctuated significantly, and was followed by a significant decreasing trend after 2007.

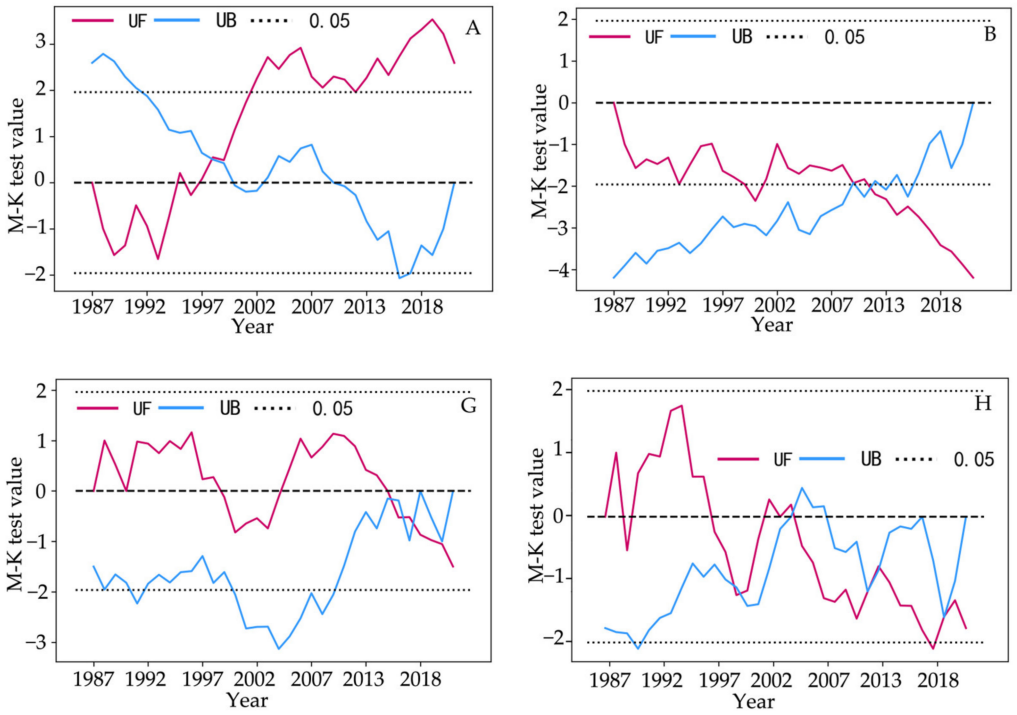

Figure 12. Temporal trend of SSC at sites A, B, G, and H (UB and UF are changing parameters where UB is the reverse of UF).

4. Discussion

4.1. The Impact of Seasonal Changes

According to the runoff and sediment load data for the past 20 years, Figure 13 indicates that the peak runoff is highly consistent with the high sediment transport, and the runoff is concentrated in the monsoon season, accounting for more than 90% of annual runoff. Sediment transport shows a seasonal trend too, and the flow in the monsoon bought a large amount of sediment to the estuary. The research shows that since the 1990s, the sediment load at the main stations of the West River has decreased significantly [34]. In Figure 13, it can be seen that the runoff from 2002 to 2020 has a trend of initial decrease and subsequent increase. The sediment load has a trend of increasing first but is followed by a decreasing trend. Wu et al. [35] pointed out that from 1994 to 2009, the sediment decreased by 83%. From 2002 to 2020, runoff and sediment load showed an opposite trend, with a decreasing trend in runoff and an increasing trend in sediment load, which suggests that the pattern of sediment load did not decrease linearly in the last decade. Then, both displayed the same trend until the end of 2015. In the following five years, from 2011 to 2016, the precipitation showed a decreasing trend, resulting in a continuous decrease in runoff and sediment load. Excluding the peak sediment load in 2017, the overall trend was decreasing.

From the cumulative departure analysis, the runoff and sediment transport showed an annual fluctuation trend, as shown in Figure 14. The trend is consistent with previous results [8]. This is directly affected by the seasonal precipitation in the Pearl River Basin. The high precipitation from March to September created peak runoff and sediment load. It is obvious that the change in sediment discharge will change according to the spatial pattern of SSC in the PRE. Due to the increased precipitation in the monsoon season, sediment discharge and runoff increased too. Therefore, the estuarine SSC in summer and autumn is significantly higher than that in winter and spring, indicating the response of SSC to the changes in sediment load. Many studies [13,22,34] have shown that the sediment loads in the PRE from the Pearl River have decreased significantly in recent decades.

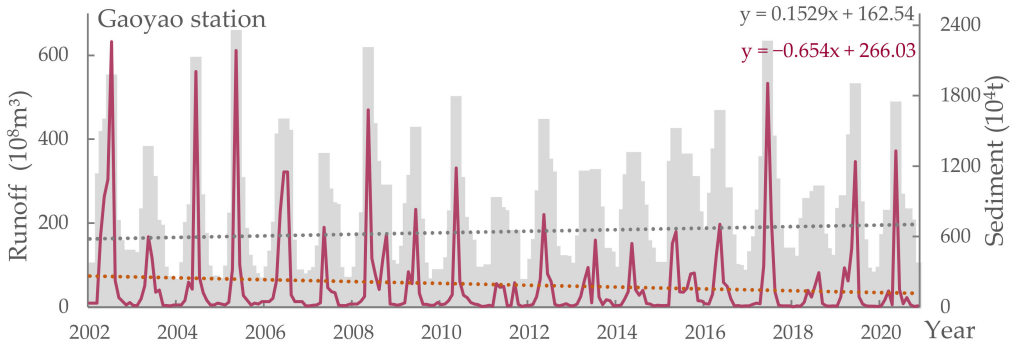

Figure 13. Runoff and sediment load at Gaoyao hydrological station, the outlet of the West River.

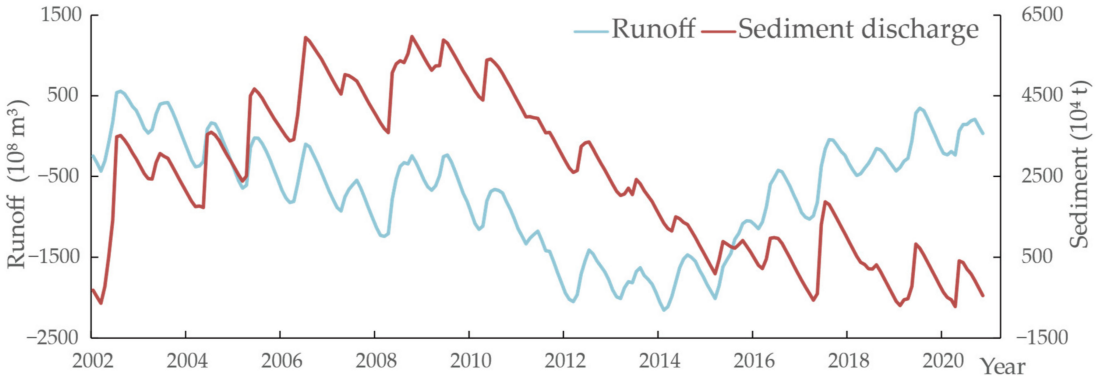

Figure 14. Cumulative departure analysis of runoff and sediment load at Gaoyao station, the outlet of the West River.

4.2. Seasonal Effects of Wind

Although the sediment in the Pearl River Estuary mainly comes from the Pearl River Basin, the wind directions can also modify the SSC by altering estuarine circulations. The winds in the monsoon season are commonly mild and mostly from the south and southwest; however, in the dry season, it is from the northeast and much stronger. Therefore, the winds can weaken or strengthen the suspension or resuspension in different seasons [36]. The predominant northeast winds in the dry season can enhance the intrusion of the surface water, while the wind-induced circulation during the monsoon season would reinforce the surface seaward flow [3].

Studies have shown that in spring, the waters in the PRE are mainly impacted by winds from the southeast, and the overall impact is relatively small due to the low wind speed [3,28]. In summer, the winds from the south become prevailing. In autumn and winter, the northeast winds are dominant. The larger the wind speed, the stronger the impact on estuarine circulations. Based on the seasonal SSC distribution in Figure 15, it can be seen that, in summer, the outside of each outlet is most affected by the runoff and sediment intake, and the waters near the outlet show a high SSC distribution. Meanwhile, under the influence of the south winds, it spread to the center of the PRE, and a large amount of sediment carried by floods into Lingding Bay led to the expansion of SSC around Inner Lingding Island. In spring, affected by both freshwater runoff and southeast winds, the SSC distribution in the estuary is mainly distributed along the west coast due to the influence of the winds [23]. When runoff decreases, the water level and SSC near outlets decrease accordingly. The sediment concentration was significantly lower than that in summer. In autumn and winter, the wind direction turns from southeast to northeast. Zhou et al. [37] also pointed out that tidal currents and strong winds in autumn and winter lead to significant resuspension. The water, driven by the winds, spreads eastward; the sediments were thus resuspended by winds and tides. The distribution of SSC gradually decreases from the west coast to Inner Lingding Island. Therefore, it can be concluded that winds can reduce/increase

the width of the surface plume frontal zone and impact the horizontal transport of the river-born suspended sediments. It can be seen in Figure 15 that the region of high SSC in the dry season is much narrower than that in the monsoon season.

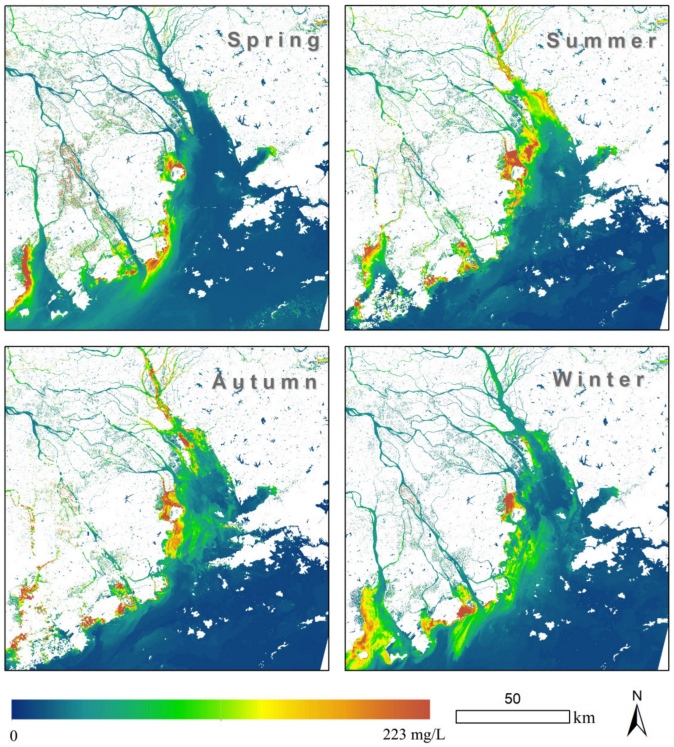

Figure 15. Distribution map of seasonal change of SSC in the PRE.

It should be emphasized that the winds' effect on the dispersion of suspended sediments develops rapidly and thus requires sensors with a high temporal resolution to capture these effects. Therefore, we just revealed a rough result in this study. More specific results could be further studied using MODIS images in the future.

4.3. Influence of Channel Dredging and Artificial Facilities

The annual dredging activities along the waterway directly affect the natural sedimentation process [38]. Normally, SSC distribution is inversely proportional to water depth, resulting in more severe nearshore siltation. The construction of large-scale water conservancy facilities in the PRE region over the past few decades has resulted in slower flow and increased siltation during the dry season. The economy has developed rapidly surrounding the PRD in the past decades.

In order to shorten the commute time on both sides of the PRE, the Hong Kong–Zhuhai–Macao Bridge and the Shenzhen–Zhongshan Tunnel (to be completed in 2024) across the PRE have been designed. The monitoring results show the SSC on both sides of the Shenzhen–Zhongshan Channel differed by more than 31.4%, as shown in Figure 16. The Hong Kong–Zhuhai–Macao Bridge, completed in 2017, has a total of 224 piers, 7 bridge towers, and 2 artificial islands with an east-to-west width of 625 m. The suspended sediment in the PRE is relatively fine, and it is susceptible to the bridge, causing the suspended sediment inside and outside the bridge to demonstrate different sediment concentrations. For example, at location F, the average sediment concentrations inside and outside the bridge are approximately 25 and 18 mg L^{-1} in autumn, respectively. A difference of 7 mg L^{-1} in sediment concentration was observed. Thus, the construction of a total of 224 piers may have a slight effect on water and sediment circulation. The difference in sediment concentration was also observed in the regions in front and back of the two

artificial islands, but the absolute difference (~3 mg L^{-1}) is not as significant as the former observation at location F (Figure 16).

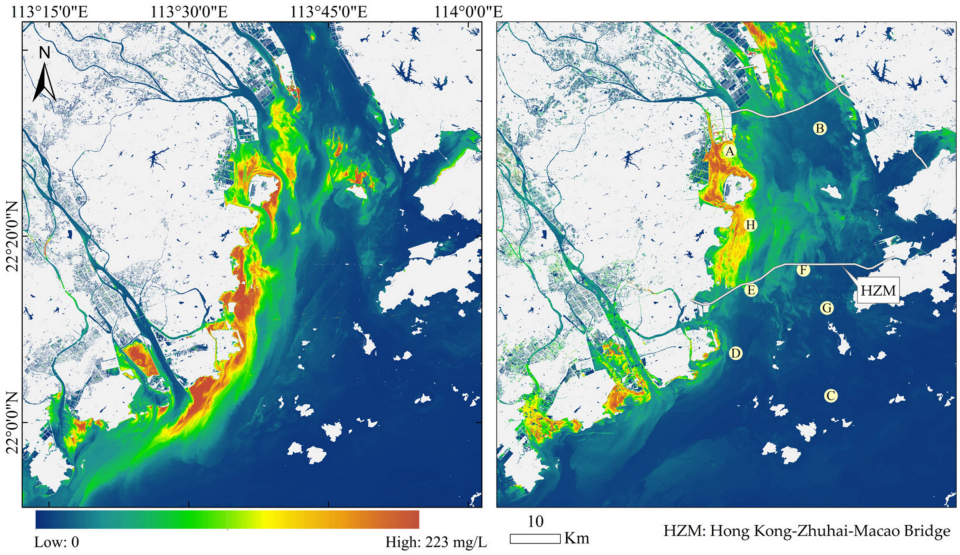

Figure 16. Impact of bridges and tunnels on the spatial distribution of SSC. (A–H) are the eight major monitoring locations selected according to SSC distribution.

4.4. Uncertainty Factors in Remote Sensing Inversion

The spectral signals of water bodies received by sensors are often affected by various factors such as the atmosphere, watershed environment, and water depth [39]. The reliability of satellite sensors, differences in sensors, atmospheric interferences, and differences in data processing methods can cause a discrepancy in SSC mapping results. However, with the introduction of new sensors and more advanced data processing methods, these errors can be gradually eliminated. The limitations of the image resolution and the inconspicuous characteristics of waters, and the mixture of spectral information in some areas can also cause a discrepancy in SSC mapping results. Using hyperspectral data can effectively improve the accuracy of SSC mapping. This will be an important research direction for SSC prediction in the future. In addition, during the mapping procedure, the sensor signal mainly comes from the surface water; therefore, it is difficult to obtain the averaged SSC for a vertical water section. Therefore, the interpretability of the measured data is affected by the sampling conditions and the scale effect of the images.

5. Conclusions

This study, taking the PRE as the study area, investigated SSC changes over the past decades by virtue of satellite images. It proved that combined with the in situ spectral data, we can effectively map SSC distribution across a large study area. The results indicated that SSC in the PRE exhibited typical periodic changes in the spatiotemporal distribution. Its spatial distribution represented a trend of high along the west coast and low along the east coast. Over the past 35 years, the SSC showed a relatively evident decreasing trend in most PRE regions, although the degree of reduction varies in different regions and needs further investigation. More attention should be paid to the decrease in SSC regarding estuary management, coastal protection, and the economic and environmental significance of estuarine sediment sustainability. The decreased sediment output from the Pearl River Basin is the major cause of the changes in SSC. However, natural factors such as wind are possible factors regulating the spatial patterns of SSC in the PRE. Human activities, such as channel dredging and the construction of artificial facilities can also disturb the spatial distribution of SSC. In the future, regions with a significant decrease in SSC, such as the region between Qi'ao Island and Inner Lingding Island and the areas along the west coasts with high SSC distribution, should receive more attention for sustainable sediment management.

Author Contributions: Conceptualization, B.C. and X.Y.; formal analysis, B.C., X.Y., J.Q. and H.L.; investigation, B.C., H.L. and W.Z.; data curation, B.C. and W.Z.; resources, B.C. and W.Z.; writing—original draft preparation, B.C.; writing—review and editing, X.Y., J.Q. and W.Z.; supervision, X.Y., X.X. and X.L. All authors have read and agreed to the published version of the manuscript.

Funding: The National Natural Science Foundation of China (Grant No.: 41871017) and the Special Fund Project for Marine Economic Development of Guangdong Province (grant number: GDNRC [2020]013) funded this research.

Data Availability Statement: The data presented in this study are available on request from the corresponding author.

Acknowledgments: The authors are very grateful to the USGS for providing the Landsat-8 OLI and Landsat-5 TM imagery. Thanks also to the European Space Agency for providing the Sentinel-2 MSI Level-2A products.

Conflicts of Interest: The authors declare no conflict of interest.

Appendix A

Table A1. In situ SSC data.

Origin ID	Longitude	Latitude	SSC (mg L^{-1})
20-07-01RS	113°44.0	22°00.7	4.0
20-07-02RS	113°44.7	22°01.6	39.7
20-07-03RS	113°42.4	22°04.1	0.7
20-07-04RS	113°40.5	22°06.1	24.3
20-07-05RS	113°38.4	22°07.9	40.7
20-07-06RS	113°39.7	22°12.9	32.7
20-07-07RS	113°38.6	22°11.3	14.7
20-07-08RS	113°37.7	22°09.8	6.3
20-07-09RS	113°37.1	22°08.7	37.7
20-07-10RS	113°36.4	22°08.0	49.6
20-07-11RS	113°36.0	22°07.2	40.3
20-07-12RS	113°35.4	22°06.6	10.0
20-07-13RS	113°34.9	22°05.8	42.7
20-07-14RS	113°34.5	22°05.0	47.7
20-07-15RS	113°35.2	22°03.8	45.7
20-07-16RS	113°35.6	22°03.0	46.7
20-07-17RS	113°36.3	22°02.4	49.7
20-07-18RS	113°36.8	22°01.8	44.0
20-07-19RS	113°37.6	22°01.4	4.7
20-07-20RS	113°38.4	22°01.2	41.3
20-07-21RS	113°39.6	22°00.0	4.3
20-07-22RS	113°41.0	21°58.9	1.3
20-07-23RS	113°42.2	21°59.2	
20-07-24RS	113°43.5	21°59.7	3.3
20-07-25RS	113°37.2	22°11.7	9.3
20-07-26RS	113°38.9	22°11.5	6.0
20-07-27RS	113°41.5	22°11.1	33.0
20-07-28RS	113°44.3	22°10.2	37.0
20-07-29RS	113°45.7	22°10.0	3.3
20-07-30RS	113°46.7	22°09.9	5.7
20-07-31RS	113°48.0	22°07.8	53.0
20-07-32RS	113°47.8	22°06.3	4.7
20-07-33RS	113°47.2	22°04.6	0.7
20-07-34RS	113°46.0	22°03.1	0.3
20-07-35RS	113°44.8	22°01.7	1.0
20-07-36RS	113°36.4	22°12.4	20.0
20-07-37RS	113°35.8	22°13.2	46.0
20-07-38RS	113°35.6	22°13.7	54.0
20-12-01RS	113.605	22.207	278.0

Table A1. *Cont.*

Origin ID	Longitude	Latitude	SSC (mg L^{-1})
20-12-02RS	113.612	22.197	232.3
20-12-03RS	113.631	22.167	288.0
20-12-04RS	113.664	22.148	129.8
20-12-05RS	113.672	22.187	169.3
20-12-06RS	113.677	22.214	189.7
20-12-07RS	113.684	22.231	180.3
20-12-08RS	113.661	22.238	103.0
20-12-09RS	113.651	22.26	162.0
20-12-10RS	113.663	22.281	84.6
20-12-11RS	113.672	22.301	80.3
20-12-12RS	113.695	22.328	54.7
20-12-13RS	113.703	22.361	53.3
20-12-14RS	113.722	22.382	57.7
20-12-15RS	113.699	22.39	46.2
20-12-16RS	113.673	22.374	
20-12-17RS	113.655	22.357	25.2
20-12-18RS	113.640	22.338	74.3
20-12-19RS	113.634	22.329	64.3
20-12-20RS	113.632	22.32	91.7
20-12-21RS	113.626	22.307	71.7
20-12-22RS	113.614	22.293	88.3
20-12-23RS	113.613	22.279	
21-04-01RS	113.655°	22.61°	67.8
21-04-02RS	113.695°	22.569°	26.6
21-04-03RS	113.724°	22.529°	14.0
21-04-04RS	113.731°	22.463°	10.6
21-04-05RS	113.743°	22.412°	21.0
21-04-06RS	113.746°	22.348°	13.6
21-04-07RS	113.727°	22.266°	28.0
21-04-08RS	113.709°	22.208°	23.8
21-04-09RS	113.691°	22.165°	17.8
21-04-10RS	113.686°	22.113°	11.6
21-04-11RS	113.679°	22.34°	18.2
21-04-12RS	113.703°	22.70°	25.0
21-04-13RS	113.747°	22.88°	/
21-04-14RS	113.751°	22.145°	/
21-04-15RS	113.725°	22.149°	13.0
21-04-16RS	113.665°	22.184°	19.2
21-04-17RS	113.603°	22.212°	14.2
21-04-18RS	113.609°	22.275°	14.2
21-04-19RS	113.630°	22.323°	23.8
21-04-20RS	113.647°	22.356°	14.2
21-04-21RS	113.673°	22.404°	16.4
21-04-22RS	113.699°	22.473°	7.4
21-04-23RS	113.71°	22.515°	
21-04-24RS	113.698°	22.567°	16.0
21-04-25RS	113.666°	22.596°	15.7
21-07-01RS	113.716°	22.538°	25.4
21-07-02RS	113.698°	22.503°	78.2
21-07-03RS	113.687°	22.476°	67.4
21-07-04RS	113.681°	22.435°	29
21-07-05RS	113.667°	22.4°	20.8
21-07-06RS	113.714°	22.441°	18
21-07-07RS	113.731°	22.485°	18
21-07-08RS	113.733°	22.523°	26.2
21-07-12RS	113.726°	22.576°	22.2

Table A2. Look-up table for the calculation of the specular reflectance of the water surface r_{sky}.

Observation Zenith Angle (°)	Relative Observation Azimuth (°) (Water Surface as the Origin)	Relative Observation Azimuth (°) (Measuring Person as the Origin)	Wind Speed (m/s)	Sun Zenith Angle (°)	Water Surface Specular Reflectance
40	45	135	0	10	0.0256
40	45	135	0	20	0.0256
40	45	135	0	30	0.0256
40	45	135	0	40	0.0256
40	45	135	0	50	0.0256
40	45	135	0	60	0.0256
40	45	135	0	70	0.0256
40	45	135	0	80	0.0256
40	45	135	2	10	0.0268
40	45	135	2	20	0.0265
40	45	135	2	30	0.0264
40	45	135	2	40	0.0264
40	45	135	2	50	0.0265
40	45	135	2	60	0.0265
40	45	135	2	70	0.0263
40	45	135	2	80	0.0262
40	45	135	4	10	0.0284
40	45	135	4	20	0.0278
40	45	135	4	30	0.0276
40	45	135	4	40	0.0277
40	45	135	4	50	0.0278
40	45	135	4	60	0.0277
40	45	135	4	70	0.0275
40	45	135	4	80	0.0272
40	45	135	6	10	0.0337
40	45	135	6	20	0.0297
40	45	135	6	30	0.029
40	45	135	6	40	0.0291
40	45	135	6	50	0.0293
40	45	135	6	60	0.0292
40	45	135	6	70	0.0289
40	45	135	6	80	0.0284
40	45	135	8	10	0.043
40	45	135	8	20	0.0335
40	45	135	8	30	0.0311
40	45	135	8	40	0.031
40	45	135	8	50	0.0312
40	45	135	8	60	0.0311
40	45	135	8	70	0.0307
40	45	135	8	80	0.03
40	90	90	0	10	0.0256
40	90	90	0	20	0.0256
40	90	90	0	30	0.0256
40	90	90	0	40	0.0256
40	90	90	0	50	0.0256
40	90	90	0	60	0.0256
40	90	90	0	70	0.0256
40	90	90	0	80	0.0256
40	90	90	2	10	0.0273
40	90	90	2	20	0.027
40	90	90	2	30	0.0267
40	90	90	2	40	0.0266
40	90	90	2	50	0.0264
40	90	90	2	60	0.0264
40	90	90	2	70	0.0263

Table A2. *Cont.*

Observation Zenith Angle (°)	Relative Observation Azimuth (°) (Water Surface as the Origin)	Relative Observation Azimuth (°) (Measuring Person as the Origin)	Wind Speed (m/s)	Sun Zenith Angle (°)	Water Surface Specular Reflectance
40	90	90	2	80	0.0262
40	90	90	4	10	0.0308
40	90	90	4	20	0.029
40	90	90	4	30	0.0278
40	90	90	4	40	0.0275
40	90	90	4	50	0.0272
40	90	90	4	60	0.0272
40	90	90	4	70	0.0271
40	90	90	4	80	0.0269
40	90	90	6	10	0.0441
40	90	90	6	20	0.0339
40	90	90	6	30	0.0293
40	90	90	6	40	0.0288
40	90	90	6	50	0.0285
40	90	90	6	60	0.0284
40	90	90	6	70	0.0283
40	90	90	6	80	0.028
40	90	90	8	10	0.0617
40	90	90	8	20	0.0448
40	90	90	8	30	0.0361
40	90	90	8	40	0.0314
40	90	90	8	50	0.0308
40	90	90	8	60	0.0306
40	90	90	8	70	0.0305
40	90	90	8	80	0.0302
0	0	0	0	10	0.0211
0	0	0	0	20	0.0211
0	0	0	0	30	0.0211
0	0	0	0	40	0.0211
0	0	0	0	50	0.0211
0	0	0	0	60	0.0211
0	0	0	0	70	0.0211
0	0	0	0	80	0.0211
0	0	0	2	10	0.2239
0	0	0	2	20	0.0865
0	0	0	2	30	0.0277
0	0	0	2	40	0.0231
0	0	0	2	50	0.0224
0	0	0	2	60	0.0219
0	0	0	2	70	0.0216
0	0	0	2	80	0.0214
0	0	0	4	10	0.1667
0	0	0	4	20	0.1316
0	0	0	4	30	0.0625
0	0	0	4	40	0.0278
0	0	0	4	50	0.0236
0	0	0	4	60	0.0226
0	0	0	4	70	0.022
0	0	0	4	80	0.0216
0	0	0	6	10	0.1259
0	0	0	6	20	0.1388
0	0	0	6	30	0.0891
0	0	0	6	40	0.0438
0	0	0	6	50	0.0246
0	0	0	6	60	0.0232

Table A2. *Cont.*

Observation Zenith Angle (°)	Relative Observation Azimuth (°) (Water Surface as the Origin)	Relative Observation Azimuth (°) (Measuring Person as the Origin)	Wind Speed (m/s)	Sun Zenith Angle (°)	Water Surface Specular Reflectance
0	0	0	6	70	0.0223
0	0	0	6	80	0.0217
0	0	0	8	10	0.1049
0	0	0	8	20	0.1276
0	0	0	8	30	0.1088
0	0	0	8	40	0.0581
0	0	0	8	50	0.033
0	0	0	8	60	0.0251
0	0	0	8	70	0.0233
0	0	0	8	80	0.0222

References

1. Curran, P.J.; Novo, E.M.M. The Relationship Between Suspended Sediment Concentration and Remotely Sensed Spectral Radiance: A Review. *J. Coast. Res.* **1988**, *4*, 351–368. [CrossRef]
2. Ritchie, J.C.; McHenry, J.R.; Schiebe, F.R.; Wilson, R.B. Relationship of reflected solar radiation and the concentration of sediment in the surface water of reservoirs. *Remote Sens. Earth Resour.* **1975**, *3*, 57–71.
3. Zhan, W.; Wu, J.; Wei, X.; Tang, S.; Zhan, H. Spatio-temporal variation of the suspended sediment concentration in the Pearl River Estuary observed by MODIS during 2003–2015. *Cont. Shelf Res.* **2019**, *172*, 22–32. [CrossRef]
4. Gholizadeh, M.; Melesse, A.; Reddi, L. A Comprehensive Review on Water Quality Parameters Estimation Using Remote Sensing Techniques. *Sensors* **2016**, *16*, 1298. [CrossRef]
5. Stumpf, R.P.; Pennock, J.R. Calibration of a general optical equation for remote sensing of suspended sediments in a moderately turbid estuary. *J. Geophys. Res.* **1989**, *94*, 14363. [CrossRef]
6. Zhang, M.; Dong, Q.; Cui, T.; Xue, C.; Zhang, S. Suspended sediment monitoring and assessment for Yellow River estuary from Landsat TM and ETM+ imagery. *Remote Sens. Environ.* **2014**, *146*, 136–147. [CrossRef]
7. Luo, W.; Shen, F.; He, Q.; Cao, F.; Zhao, H.; Li, M. Changes in suspended sediments in the Yangtze River Estuary from 1984 to 2020: Responses to basin and estuarine engineering constructions. *Sci. Total Environ.* **2022**, *805*, 150381. [CrossRef]
8. Wang, C.; Li, W.; Chen, S.; Li, D.; Wang, D.; Liu, J. The spatial and temporal variation of total suspended solid concentration in Pearl River Estuary during 1987–2015 based on Remote Sens. *Sci. Total Environ.* **2018**, *618*, 1125–1138. [CrossRef]
9. Qiu, Z.; Xiao, C.; Perrie, W.; Sun, D.; Wang, S.; Shen, H.; Yang, D.; He, Y. Using Landsat 8 data to estimate suspended particulate matter in the Yellow River estuary: Landsat 8 spm in the yellow river estuary. *J. Geophys. Res. Ocean.* **2017**, *122*, 276–290. [CrossRef]
10. Cheng, Z.; Wang, X.; Paull, D.; Gao, J. Application of the Geostationary Ocean Color Imager to Mapping the Diurnal and Seasonal Variability of Surface Suspended Matter in a Macro-Tidal Estuary. *Remote Sens.* **2016**, *8*, 244. [CrossRef]
11. Peterson, K.; Sagan, V.; Sidike, P.; Cox, A.; Martinez, M. Suspended Sediment Concentration Estimation from Landsat Imagery along the Lower Missouri and Middle Mississippi Rivers Using an Extreme Learning Machine. *Remote Sens.* **2018**, *10*, 1503. [CrossRef]
12. Chelotti, G.B.; Martinez, J.M.; Roig, H.L.; Olivietti, D. Space-Temporal analysis of suspended sediment in low concentration reservoir by Remote Sens. *RBRH* **2019**, *24*, 143–151. [CrossRef]
13. Wu, Z.; Milliman, J.D.; Zhao, D.; Cao, Z.; Zhou, J.; Zhou, C. Geomorphologic changes in the lower Pearl River Delta, 1850–2015, largely due to human activity. *Geomorphology* **2018**, *314*, 42–54. [CrossRef]
14. Qiu, J.; Cao, B.; Park, E.; Yang, X.; Zhang, W.; Tarolli, P. Flood Monitoring in Rural Areas of the Pearl River Basin (China) Using Sentinel-1 SAR. *Remote Sens.* **2021**, *13*, 1384. [CrossRef]
15. Yang, X.; Lu, X.; Ran, L.; Tarolli, P. Geomorphometric Assessment of the Impacts of Dam Construction on River Disconnectivity and Flow Regulation in the Yangtze Basin. *Sustainability* **2019**, *11*, 3427. [CrossRef]
16. Yang, X.; Lu, X.X. Estimate of cumulative sediment trapping by multiple reservoirs in large river basins: An example of the Yangtze River basin. *Geomorphology* **2014**, *227*, 49–59. [CrossRef]
17. Wu, Z.; Zhao, D.; Syvitski, J.P.M.; Saito, Y.; Zhou, J.; Wang, M. Anthropogenic impacts on the decreasing sediment loads of nine major rivers in China, 1954–2015. *Sci. Total Environ.* **2020**, *739*, 139653. [CrossRef]
18. Li, P.; Ke, Y.; Bai, J.; Zhang, S.; Chen, M.; Zhou, D. Spatiotemporal dynamics of suspended particulate matter in the Yellow River Estuary, China during the past two decades based on time-series Landsat and Sentinel-2 data. *Mar. Pollut. Bull.* **2019**, *149*, 110518. [CrossRef]
19. Gao, F.; Wang, Y.; Hu, X. Evaluation of the suitability of Landsat, MERIS, and MODIS for identifying spatial distribution patterns of total suspended matter from a self-organizing map (SOM) perspective. *CATENA* **2019**, *172*, 699–710. [CrossRef]

20. Du, Y.; Lin, H.; He, S.; Wang, D.; Wang, Y.P.; Zhang, J. Tide-Induced Variability and Mechanisms of Surface Suspended Sediment in the Zhoushan Archipelago along the Southeastern Coast of China Based on GOCI Data. *Remote Sens.* **2021**, *13*, 929. [CrossRef]
21. Mao, Q.; Shi, P.; Yin, K.; Gan, J.; Qi, Y. Tides and tidal currents in the Pearl River Estuary. *Cont. Shelf Res.* **2004**, *24*, 1797–1808. [CrossRef]
22. Dai, S.B.; Yang, S.L.; Cai, A.M. Impacts of dams on the sediment flux of the Pearl River, southern China. *CATENA* **2008**, *76*, 36–43. [CrossRef]
23. Ou, S.; Yang, Q.; Luo, X.; Zhu, F.; Luo, K.; Yang, H. The influence of runoff and wind on the dispersion patterns of suspended sediment in the Zhujiang (Pearl) River Estuary based on MODIS data. *Acta Oceanol. Sin.* **2019**, *38*, 26–35. [CrossRef]
24. Mobley, C.D. Estimation of the remote-sensing reflectance from above-surface measurements. *Appl. Opt.* **1999**, *38*, 7442. [CrossRef] [PubMed]
25. Tang, J.; Tian, G.; Wang, X. Spectral Measurement and Analysis of Water I: Above-water Measurement. *Natl. Remote Sens. Bull.* **2004**, *8*, 37–44.
26. Li, H.; Xie, X.; Yang, X.; Cao, B.; Xia, X. An Integrated Model of Summer and Winter for Chlorophyll-a Retrieval in the Pearl River Estuary Based on Hyperspectral Data. *Remote Sens.* **2022**, *14*, 2270. [CrossRef]
27. Zhao, J.; Zhang, F.; Chen, S.; Wang, C.; Chen, J.; Zhou, H.; Xue, Y. Remote Sensing Evaluation of Total Suspended Solids Dynamic with Markov Model: A Case Study of Inland Reservoir across Administrative Boundary in South China. *Sensors* **2020**, *20*, 6911. [CrossRef]
28. Jia, Q.; Zhang, G.; Tang, S.; Zhang, H. Analysis on seasonal changes of suspended sediment in Lingdingyang waters of the Pearl River Estuary from 2013 to 2018. *J. Sun Yat-Sen Univ.* **2021**, *60*, 59–71. [CrossRef]
29. Wang, J.-J.; Lu, X.X.; Liew, S.C.; Zhou, Y. Retrieval of suspended sediment concentrations in large turbid rivers using Landsat ETM+: An example from the Yangtze River, China. *Earth Surf. Processes Landf.* **2009**, *34*, 1082–1092. [CrossRef]
30. Collins, M.; Pattiaratchi, C. Identification of suspended sediment in coastal waters using airborne thematic mapper data. *Int. J. Remote Sens.* **1984**, *5*, 635–657. [CrossRef]
31. Islam, M.R.; Yamaguchi, Y.; Ogawa, K. Suspended sediment in the Ganges and Brahmaputra Rivers in Bangladesh: Observation from TM and AVHRR data. *Hydrol. Processes* **2001**, *15*, 493–509. [CrossRef]
32. Wang, S.; Li, J.; Zhang, B.; Shen, Q.; Zhang, F.; Lu, Z. A simple correction method for the MODIS surface reflectance product over typical inland waters in China. *Int. J. Remote Sens.* **2016**, *37*, 6076–6096. [CrossRef]
33. MWR.CN. China River Sediment Bulletin 2001–2020. 2021. Available online: http://www.pearlwater.gov.cn/zwgkcs/lygb/nsgb/202111/P020211126575293575253.pdf (accessed on 12 June 2022).
34. Zhang, S.; Lu, X.X.; Higgitt, D.L.; Chen, C.-T.A.; Han, J.; Sun, H. Recent changes of water discharge and sediment load in the Zhujiang (Pearl River) Basin, China. *Glob. Planet Chang.* **2008**, *60*, 365–380. [CrossRef]
35. Wu, C.S.; Yang, S.L.; Lei, Y.-P. Quantifying the anthropogenic and climatic impacts on water discharge and sediment load in the Pearl River (Zhujiang), China (1954–2009). *J. Hydrol.* **2012**, *452–453*, 190–204. [CrossRef]
36. Scully, M.E.; Friedrichs, C.; Brubaker, J. Control of estuarine stratification and mixing by wind-induced straining of the estuarine density field. *Estuaries* **2005**, *28*, 321–326. [CrossRef]
37. Zhou, Y.; Xuan, J.; Huang, D. Tidal variation of total suspended solids over the Yangtze Bank based on the geostationary ocean color imager. *Sci. China Earth Sci.* **2020**, *63*, 1381–1389. [CrossRef]
38. Wu, Z.Y.; Saito, Y.; Zhao, D.N.; Zhou, J.Q.; Cao, Z.Y.; Li, S.J.; Shang, J.H.; Liang, Y.Y. Impact of human activities on subaqueous topographic change in Lingding Bay of the Pearl River estuary, China, during 1955–2013. *Sci. Rep.* **2016**, *6*, 37742. [CrossRef]
39. Chen, J.; Chen, S.; Fu, R.; Li, D.; Jiang, H.; Wang, C.; Peng, Y.; Jia, K.; Hicks, B.J. Remote Sensing Big Data for Water Environment Monitoring: Current Status, Challenges, and Future Prospects. *Earth's Future* **2022**, *10*, e2021EF002289. [CrossRef]